A practical and efficient asymptotic coarse-graining model for the elastohydrodynamics of slender-rods and filaments

Clément Moreau, Laetitia Giraldi, Hermes Gadêlha

A practical and efficient asymptotic coarse-graining model for the elastohydrodynamics of slender-rods and filaments

Clément Moreau[1], Laetitia Giraldi[1], and Hermes Gadêlha[2*]
[1] *Université Côte d'Azur, Inria, CNRS, LJAD, McTAO team, France*
[2] *Department of Mathematics, University of York, YO10 5DD, UK*
(Dated: December 7, 2017)

The inertialess fluid-structure interaction of active and passive inextensible filaments and slender-rods are central in many processes in nature, from the dynamics of semi-flexible polymers to cytoskeletal filaments, flagella and artificial swimmers, covering a wide range of scales. The nonlinear coupling between the geometry of deformation and the physical effects invariably result on intricate governing equations that negotiate elastohydrodynamical interactions with non-holonomic constraints, as a direct consequence of the filament inextensibility. This triggers numerical instabilities and require penalization methods and high-order spatiotemporal propagators. Here, we exploit the the momentum balance in the asymptotic limit of small rod-like elements which are integrated semi-analytically. This bypasses the nonlinearities arising via the inextensibilty constraint, avoiding in this way the need of Langrange multipliers. The equivalence between the continuous and asymptotic model allows a direct comparison between the two formalisms. The nature of the asymptotic approximation entails that coarse discretisation is possible while having a higher precision when compared with the continuous approach. We show that the asymptotic model is also numerically stable in situations in which the continuous formalism has a very poor performance, while the coarse structure guarantees faster computations, over than a hundred times faster than previous schemes. The asymptotic model is simple and intuitive to implement, and generalisations for complex interaction of multiple rods, Brownian polymer dynamics, active filaments and non-local hydrodynamics are straightforward. We demonstrate these via four exemplars: transient dynamics, force-displacement buckling instability, magnetic artificial swimmer and cross-linked filament-bundle dynamics, and we additionally provide the Matlab codes.

I. INTRODUCTION

The fluid-structure interaction of semi-flexible filaments are found everywhere in nature [1–3]. From mechanics of DNA strands and the movement of polymer chains to complex cytoskeletal microtubule and actin cross-linking architectures to statics and dynamics of filament-bundles whose ability to self-organize and coordinate movement is observed in spermatozoa movement [4–18]. The elastohydrodynamics of filaments permeate through different branches in mathematical sciences, physics and engineering, and their cross-fertilizing intersects with biology, chemistry and even industry. The wealth of theoretical and experimental studies on the movement of semi-flexible filaments, termed here as filaments, is extensive, thus reflecting the fundamental importance of the physical interactions marring fluid and elastic phenomena. Hitherto the elastohydrodynamics of active and passive filaments have shed new light into bending, buckling, active matter and self-organisation, as well as bulk material properties of interacting active and passive fibres across disciplines [4–13, 19].

The movement of semi-flexible filaments brings together complex fluid and elastic interactions with a hierarchy of different approximations [20]. Here, we focus our study on systems governed by low Reynolds number inertialess hydrodynamics [21]. Both the hydrodynamic and elastic interactions of filaments are greatly simplified by exploiting the filament slenderness [1, 20], reducing the dynamics to effectively an one-dimensional system [22]. A variety of model families have been developed exploiting such slenderness property, and thus it would be a challenging task to review the wealth of theoretical and empirical developments to date here. Instead we direct the reader to excellent reviews on the subject [23–26]. We consider the dynamics of inextensible elastic filaments constrained to planar deformations. In a nutshell, two theoretical descriptions are popularly used: the discrete and continuous formulation. Discrete models, such as the beads model, gears model, n-links model, or similarly worm-like chain models, the filament is broken into a discrete number of units, such as straight segments, spheres or ellipsoids. The elastic interaction coupling neighboring nodes/joints are encoded via a constitutive energy functionals or via a discrete elastic connectors encoding the filament's resistance to bending. The shape of each constituent discrete unit defines the underlaying approximation for the hydrodynamical interaction, i.e. sphere hydrodynamics for the beads and gears model, and slender-body hydrodynamics for straight filaments. The dynamics is governed by enforcing force and torques balance for each node. Continuous models, on the other hand, recur to partial differential equation (PDE) system to describe the combined action from fluid-structure interactions [11, 27], the dynamics arises through the total balance of contact forces and contact moments along the filament [1]. This formalism results invariably in a nonlinear PDE system coupling a hypediffusive fourth-

* hermes.gadelha@york.ac.uk

order PDE with a second-order boundary value problem (BVP) required to ensure inextensibility via the line tension [4, 11, 27], in addition to six boundary conditions and associated initial configuration for closeness. The geometrical coupling guarantees that the order of the PDE remains unchanged under transformation of variables, from the position of filament centreline $X(s,t)$ at an arclength s and time t relative to a fixed frame of reference, to tangent angle $\theta(s,t)$ or curvature $\kappa(s,t)$ of the filament.

While equivalence between discrete and continuum models is generally not available, both theoretical frameworks suffer from numerical instability and stiffness arising from the nonlinear geometrical coupling between the filament's curvature and its inextensibility constraint [11]. Nonlinearities originated from curvature are well known to drive numerical instability in moving boundary systems, as found in pattern formation of interfacial flows driven by surface tension, as well as in elastic and fluid stresses in shells and fluid membranes. The latter often requires numerical regularization, such as the small-scale decomposition. Contact forces of inexstensible filaments are not determined constitutively. This requires the action of Lagrange multipliers to ensure the strict length constraint, thus inducing in both discrete and continuous models numerical instabilities. This is despite the fact that, for instance, discrete models automatically satisfy the length constraint by construction, or equivalently the tangent angle formulation $\theta(s,t)$ in continuous models, which preserves lengths by definition. The issue is due to the fact that the unknown tension line distribution is still required to resolve the underlaying filament dynamics. In continuum models, penalization strategies are often required to regularize length errors that are augmented at each time step. Finally, the inextensibility constraint in PDE models unnecessarily increase the number of boundary conditions required to closeness, thus preventing this formalism for problems involving more complex boundary conditions, as we discuss bellow. The latter causes imposes severe spatiotemporal discretization constraints, augmenting not only the computational time for non-linearities triggered by high curvature, but also the associated numerical errors. Other strategy is to enforce inextensibility indirectly, by considering instead an extensible filament characterised by constitutive relations encoding large resistance to compression/extension. This method increases the number of strain variables to keep track during the dynamics, whilst the system is still prone to numerical instability and length variations near inextensible regime.

The aim of this paper is to resolve the current bottleneck of interaction between the hyperdiffusive elastohydrodynamic coupling and the inextensibility constraint. For this we consider a hybrid continuum-discrete approach. Our starting point is the continuum formalism, from which the total balance of contact forces and moments can be integrated asymptotically for a coarse rod-like discretization, thus automatically encoding inextensibility and preventing the need for an explicit length constraint. This results in linear system that couples all constituent elements along the filament via the total momentum balance which can be readily solved numerically, without requiring explicit computation of unknown internal forces afore mentioned. This hybrid continuum-discrete method arises through the asymptotic integration of the moment balance system, instead of mapping the system into a higher order system of partial differential equations (PDE). This greatly decreases the implementation complexity, the number of boundary conditions required, computational time and numerical stiffness. The simplicity of such hybrid framework allows its application to systems that would be prohibitive using previous models.

We contrast the continuous differential model with the asymptotic approach. The asymptotic model is observed to be numerically stable in situations in which the continuous formalism has a very poor performance. The coarse structure of the linear system also results in faster computations, over than a hundred times faster, with increasingly better performance for tolerance to error below that 1%. Furthermore, we show that the asymptotic model is simple and intuitive to implement, and generalisations for complex interaction of multiple rods, Brownian polymer dynamics, active filaments and non-local hydrodynamics are straightforward. We demonstrate these via four exemplars: transient dynamics, force-displacement buckling instability, magnetic artificial swimmer and cross-linked filament-bundle dynamics, and we additionally provide the Matlab codes.

The paper is structured as follows: First we describe the momentum balance for an inextensible filament embedded in a inertialess fluid and derive the elastohydrodynamic system and the associated asymptotic approximation in Section II, based on the standard elastic rod theory and lowest order approximation for the slender-body hydrodynamics. In Section III, we contrast the the elastohydrodynamic and the assympotitic model and their respective performances. Finally, we abandon the elastohydrodynamic euqations and present several applications of the asymptotic model that would be prohibitive otherwise in Section IV: the buckling instability, magnetic-driven micro-swimmers and the counter-bend phenomenon in filament-bundles [28]. All Matlab codes are provided in github free repository.

II. THE ELASTOHYDRODYNAMIC FILAMENT THEORY

Consider an inextensible elastic rod of length L, parametrized by its arclength. The position of a point of arclength s on the filament is denoted by $\mathbf{x}(s)$. Two types of forces are applied to the rod [1]: contact forces $\mathbf{n}(s)$, induced by the filament itself, and external forces, that have a force density $\mathbf{f}(s)$ (by unit of length), later this will incorporate the hydrodynamic effects. The sec-

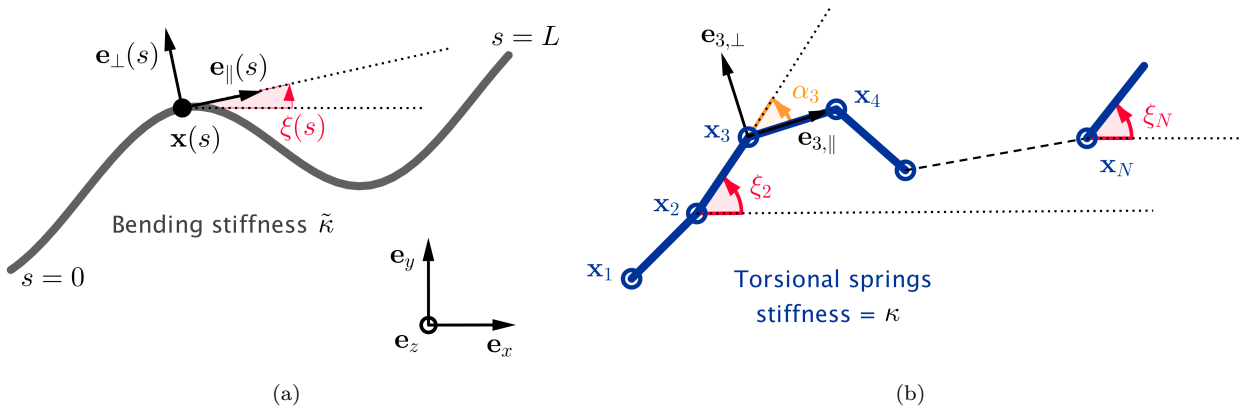

(a) (b)

FIG. 1. Parametrization of the continuous and discrete filaments

ond Newton's law ensures the balance of forces and moments:

$$\mathbf{n}_s + \mathbf{f} = 0, \tag{1}$$

$$\mathbf{m}_s + \mathbf{x}_s \times \mathbf{n} + \mathbf{p} = 0, \tag{2}$$

where the subscripts denote derivatives with respect to arclength s, $\mathbf{m}(s)$ is the contact moment, $\mathbf{p}(s)$ is the external moment. The dynamical system (1)-(2) is further specified by the geometry of the deformation and the constitutive relations characterising the elastic properties of this he filament. Here we focus on inextensible, unshearable hyperelastic filaments undergoing planar deformations. Thus the contact forces are not defined constitutively whilst the bending moment is linearly related to the local curvature.

The position of the filament centreline is denoted by $\mathbf{x}(t, s)$. The Frenet basis moving with the filament is given by $(\mathbf{e}_\parallel, \mathbf{e}_\perp)$, tangent and normal vector respectively. The angle between the x-axis of frame of reference and $\mathbf{e}_\parallel$ is θ, where the normal vector to the plane in which deformation occurs is $\mathbf{e}_z$, see Figure 1. The filament is characterised by a bending stiffness E_b, and thus elastic moments are simply $\mathbf{m}(s) = E_b\theta_s\mathbf{e}_z$. The latter can be used in conjuction with (2), using $\theta_{ss}\mathbf{e}_\perp = \mathbf{x}_{sss}$, to get

$$\mathbf{n}(s) = -E_b\mathbf{x}_{sss}\mathbf{e}_\perp + \tau\mathbf{e}_\parallel,$$

where $\tau(s)$ is the unknown Lagrange multiplier. The hydrodynamical friction experienced by a slender-body in low Reynolds number regime can be simplified to the asymptotically by employing the Resistive Force Theory [29], in which hydrodynamic friction is related with to velocity via an anisotropic operator

$$\mathbf{f} = -(\xi\mathbf{e}_\perp \cdot \mathbf{e}_\perp + \eta\mathbf{e}_\parallel \cdot \mathbf{e}_\parallel)\mathbf{x}_t,$$

where η and ξ are the parallel and perpendicular restive coefficients, respectively. Using (1) and nondimensionalizing the system with respect to the length scale L, time scale ω^{-1}, force density E_b/L^3, and noticing that $\mathbf{e}_\parallel = \mathbf{x}_s$, the dimensionless elatohydrodynamic equation for a passive filament deforming in a viscous environment reads:

$$\mathrm{Sp}^4\mathbf{x}_t = -\mathbf{x}_{ssss} - (\gamma - 1)(\mathbf{x}_s \cdot \mathbf{x}_{ssss})\mathbf{x}_s + (\tau\mathbf{x}_{ss} + \gamma\tau_s\mathbf{x}_s), \tag{3}$$

with the dimensionless parameters $\mathrm{Sp} = L(\omega\xi/E_b)^{1/4}$ and $\gamma = \xi/\eta$. The unknown line tension is obtained by invoking the inextensibility constraint

$$\frac{\partial}{\partial t}(\mathbf{x}_s \cdot \mathbf{x}_s) = 0, \tag{4}$$

which together with (3) provides a nonlinear second-order boundary value problem for the line tension,

$$\gamma\tau_{ss} - (\mathbf{x}_{ss}\cdot\mathbf{x}_{ss})\tau = -3\gamma(\mathbf{x}_{sss}\cdot\mathbf{x}_{sss}) - (3\gamma+1)(\mathbf{x}_{ss}\cdot\mathbf{x}_{ssss}). \tag{5}$$

In practice, however, the inextensibility condition above is prone to numerical erros [11] causing the filament length to vary over time. A penalisation term is thus added on the right-hand side of (4) to remove spurious incongruousnesses of the tangent vector [11].

The non-linear, geometrically exact elastohydrodynamical system Eqs. (3) and (5) requires a set initial and boundary conditions for closeness. At the filament boundaries force and torque balance or the endpoints movements are specified. Here we consider the distal end free from external forces and moments

$$\forall t, \quad -\mathbf{x}_{sss}(t, L) + \tau\mathbf{x}_s(t, L) = 0, \quad \mathbf{x}_{ss}(t, L) = 0.$$

At the proximal end, several scenarios may be considered: (i) Free torque and force condition, thus the above equations is applied at $s = 0$. (ii) Pivoting, pinned or hinged condition: the extremity has a fixed position but it is free rotate around it, $\mathbf{x}_t(t, 0) = 0, \mathbf{x}_{ss}(t, 0) = 0$. (iii) Clamped condition: the extremity has a fixed position and orientation, $\mathbf{x}_t(t, 0) = 0, \mathbf{x}_{st}(t, 0) = 0$. Finally, initial conditions are required for further closeness of the elastohydrodynamic system. Boundary conditions for the tension line

(5) boundary value system are derived from the above constraint accordingly. The boundary constraints for τ are generally unknown, coupling simultaneously (3) and (5).

Numerical scheme for the PDE system

The equations (3) and (5) contain fourth-order derivatives of $\mathbf{x}$, and are therefore numerically challenging. The numerical scheme proposed in [30] uses an implicit-explicit scheme (more details below). The results obtained have been validated against known numerical solutions, and experimental data (in particular for a periodically actuated filament, see [30]) with very good accuracy in most cases. However, a few issues remain:

- As stated above, when solved numerically, the total length of the filament does not remain perfectly constant due to the inevitable numerical errors induced by the high-order terms in both equations. This length variation is negligible if the curvature of the filament is small enough but can become problematic for sharp curvatures.
- In the case of a floppy filament (high Sp number), the scheme works very quickly, i.e. the time and space steps do not have to be very small. But lower sperm numbers are not well supported by the solver. One has to unreasonably decrease the time step in order for the solution to converge, leading to very long computing times.
- Some boundary conditions may be hard to embed in the system, because they would need to know unknown forces applied at the filament ends.

Overall, the PDE model lacks robustness, accuracy, and versatility. In the following section, we present a model based on a discretized filament, that leads to a system of ordinary differential equations. We will then confront the two models and compare their numerical performances.

A. From continuous to discrete ODE model

We now describe a second model for an elastic filament. This time, it is a "discrete" filament made of N rigid segments. This model has been introduced in [31] and [32]. We will widely use their notations in what follows.

Consider a filament of length L consisting on N rigid segments connected on each other by torsional springs with stiffness κ. These torsional springs play the role of the bending stiffness for the continuous elastic filament studied above.

The N segments, called S_i for $i \in \{1, \dots, N\}$, have same length $\ell = \Delta s = L/N$ and same hydrodynamic drag coefficients ξ and η. The filament can move in the 2d-plane defined by the vectors $\mathbf{e}_x$ and $\mathbf{e}_y$. Let us define $\mathbf{e}_z = \mathbf{e}_x \times \mathbf{e}_y$.For each $i \in \{1, \dots, N\}$, we define $\mathbf{x}_i = \mathbf{x}((i-1)/N) = (x_i, y_i)$ the coordinates of the end of S_i, $(\mathbf{e}_{i,\parallel}, \mathbf{e}_{i,\perp})$ the orthonormal basis associated to S_i and θ_i the angle between $\mathbf{e}_x$ and $\mathbf{e}_{i,\parallel}$. Finally, we set $\alpha_1 = \theta_1$ and, for $i \in \{2, \dots, N\}$, we define α_i as the angle between $\mathbf{e}_{i-1,\parallel}$ and $\mathbf{e}_{i,\parallel}$, i.e. $\alpha_i = \theta_i - \theta_{i-1}$.

Figure 1 shows all these parameters on a picture. Moreover, for every $i \in \{2, \dots, n\}$, one has the following kinematic relations:

$$\begin{aligned} \alpha_i &= \theta_i - \theta_{i-1} \\ \theta_i &= \textstyle\sum_{k=1}^{i} \alpha_k \\ x_i &= x_1 + \textstyle\sum_{k=1}^{i-1} \ell \cos\theta_k \\ y_i &= y_1 + \textstyle\sum_{k=1}^{i-1} \ell \sin\theta_k \end{aligned}$$

A few more details about the parametrization are given in Appendix VI A.

The filament is fully described by the $N+2$ parameters $(x_1, y_1, \alpha_1, \alpha_2, \dots, \alpha_N)$: the coordinates of the first end, and one "shape" angle for each segment. In order to solve the dynamics of this filament, we are therefore going to write $N+2$ scalar equations.

As previously, we can apply Newton's laws to the filament. The balance of forces (similar to (1)) over the whole filament reads

$$\mathbf{n}(L) - \mathbf{n}(0) + \int_0^L \mathbf{f}(s) ds = 0.$$

Since there are no contact forces at the ends of the filament, $\mathbf{n}(L) = \mathbf{n}(0) = 0$. We separate the integral over each link to get

$$\sum_{i=1}^{N} \int_{(i-1)\Delta s}^{i\Delta s} \mathbf{f}(s) ds = 0.$$

The quantity $\int_{(i-1)\Delta s}^{i\Delta s} \mathbf{f}(s) ds$ represents force applied to the i-th segment. Let us call it, naturally, $\mathbf{F}_i^h$. Hence we get the first equation :

$$\sum_{i=1}^{N} \mathbf{F}_i^h = 0. \tag{6}$$

This first vectorial equation gives two scalar equations (by projecting on x- and y-axis). We need N more to be able to solve the dynamics. To this purpose, we write the balance of moments over N different parts of the filament, giving N independent equations. In order to take into account the elastic contribution at each link junction, we will consider the whole filament, and subsystems $\{S_i + S_{i+1} + \dots + S_N\}$ for $i \in \{2, \dots, N\}$. Each of these subsystems represents a part of the discrete filament that goes from the i-th link to the end of the filament – therefore allowing the elastic effects to appear in the equations. This set of subsystems is not the only one that would lead to N independent equations. We chose it over others because it yields a relatively simple

equation system, due to the fact that every subsystem in it has a free end.

For the whole filament, since $\mathbf{m}(L) = \mathbf{m}(0) = 0$, and assuming there are no external moments ($\mathbf{p} = 0$), we get

$$\sum_{i=1}^{N} \int_{(i-1)\Delta s}^{i\Delta s} \mathbf{x}'(s) \times \mathbf{n}(s) ds = 0.$$

We then integrate by parts to get

$$\sum_{i=1}^{N} \Big(\Big[(\mathbf{x}(s) - \mathbf{x}_1) \times \mathbf{n}(s) \Big]_{i\Delta s}^{(i+1)\Delta s} - \int_{(i-1)\Delta s}^{i\Delta s} (\mathbf{x}(s) - \mathbf{x}_1) \times \mathbf{n}'(s) ds \Big) = 0.$$

Similarly to above, we denote by $\mathbf{M}^h_{i+1,\mathbf{x}_1}$ the quantity $\int_{i\Delta s}^{(i+1)\Delta s} (\mathbf{x}(s) - \mathbf{x}_1) \times \mathbf{n}'(s)$, which is the torque applied to the segment S_i, with respect to the point $\mathbf{x}_1$, hence the $\mathbf{x}_1$ subscript. The nonintegral terms in the sum cancel each other, yielding the second equation:

$$\sum_{i=1}^{N} \mathbf{M}^h_{i,\mathbf{x}_1} = 0. \tag{7}$$

Let $j \in \{2, \dots, N\}$. We repeat the integration of (2), this time over the subsystem $\{S_j + S_{j+1} + \dots + S_N\}$ and integrate by parts to get a balance of torques equation, with respect to $\mathbf{x}_j$:

$$-\mathbf{M}(j\Delta s) + \sum_{i=j}^{N} \mathbf{M}^h_{i,\mathbf{x}_j} = 0. \tag{8}$$

Here, the term $-\mathbf{M}(j\Delta s)$ is the elastic contribution from the torsional spring at the j-th link. Let us therefore call it $\mathbf{M}^{\text{el}}_j$. With equations (6), (7) and (8) for $j \in \{2 \dots N\}$, we obtain a system of $N+1$ equations that reads

$$\begin{cases} \sum_{i=1}^{N} \mathbf{F}^h_i &= 0 \\ \sum_{i=1}^{N} \mathbf{M}^h_{i,\mathbf{x}_1} &= 0 \\ \sum_{i=2}^{N} \mathbf{M}^h_{i,\mathbf{x}_2} &= -\mathbf{M}^{\text{el}}_2 \\ \vdots & \vdots \quad \vdots \\ \mathbf{M}^h_{N,\mathbf{x}_N} &= -\mathbf{M}^{\text{el}}_N \end{cases} \tag{9}$$

This system gives $N+2$ scalar equations by projecting the first line on (Ox) and (Oy) and the N others on (Oz). Let us emphasize on the fact that this system allows to solve the dynamics of the filament. In the PDE case, the inextensibility equation (4) is needed in addition. In this model, the inextensibility is intrisic.

From this system, we can express every term with respect to the parameters. As for the equations (1) to (2), they will depend on the assumptions made: we will use the Resistive Force Theory here for the hydrodynamics, and use a linear torsional spring term to model the contact force between links as stated before, but other expressions could be considered. For example, in the case of a filament moving close to a wall, the hydrodynamics change; then another expression would have to be chosen for the hydrodynamic contributions in (9). Nonlinear elasticity effects could be taken into account as well.

Since the Reynolds number is low enough, we can assume that the system is in Stokes regime, hence the speed of displacement depends linearly on the forces, and we are able to express the system (9) with respect to the derivatives of the parameters $(\dot{x}_i, \dot{y}_i, \dot{\alpha}_i)$ as follows. This will allow to implement a numerical scheme.

Hydrodynamics

As before, we assume that the dynamics stands within the frame of the Resistive Force Theory (see [29]). Therefore, the drag force per unit length intensity is proportional to the velocity and to the hydrodynamics coefficients ξ and η. Again, we take $\gamma = \xi/\eta$. Let $\mathbf{x}(s)$ be a point on one of the segments S_i. In the moving frame $(\mathbf{e}_{i,\parallel}, \mathbf{e}_{i,\perp})$, the drag force exerted on this point reads

$$\mathbf{f}_i(\mathbf{x}(s)) = -\xi(\dot{\mathbf{x}}(s) \cdot \mathbf{e}_{i,\parallel})\mathbf{e}_{i,\parallel} - \eta(\dot{\mathbf{x}}(s) \cdot \mathbf{e}_{i,\perp})\mathbf{e}_{i,\perp}$$

We have $u_{i,\parallel}(s) = \dot{\mathbf{x}}(s).\mathbf{e}_{i,\parallel}$ and $u_{i,\perp}(s) = \dot{\mathbf{x}}(s).\mathbf{e}_{i,\perp}$. Hence, the hydrodynamic force $\mathbf{F}^h_i$ exerted on S_i is given by :

$$\begin{aligned} \mathbf{F}^h_i &= \int_{S_i} \mathbf{f}_i(\mathbf{x}(s)) ds \\ &= \int_{(i-1)\Delta s}^{i\Delta s} \big(-\xi(\dot{\mathbf{x}}(s) \cdot \mathbf{e}_{i,\parallel})\mathbf{e}_{i,\parallel} - \eta(\dot{\mathbf{x}}(s) \cdot \mathbf{e}_{i,\perp})\mathbf{e}_{i,\perp} \big)\, ds. \end{aligned}$$

Since that

$$\dot{\mathbf{x}}(s) = \begin{pmatrix} \dot{x}_i - (s - (i-1)\Delta s)\dot{\theta}_i \sin\theta_i \\ \dot{y}_i + (s - (i-1)\Delta s)\dot{\theta}_i \cos\theta_i \end{pmatrix},$$
$$\mathbf{e}_{i,\parallel} = \begin{pmatrix} \cos\theta_i \\ \sin\theta_i \end{pmatrix}, \mathbf{e}_{i,\perp} = \begin{pmatrix} -\sin\theta_i \\ \cos\theta_i \end{pmatrix}$$

in the reference frame, the force reads after calculating the integral

$$\begin{aligned} \mathbf{F}^h_i &= \eta \Delta s\, G(\theta_i)^T \begin{pmatrix} \dot{x}_i \\ \dot{y}_i \\ \Delta s\, \dot{\theta}_i \end{pmatrix}, \\ G(\theta) &= \begin{pmatrix} -\cos^2\theta - \gamma \sin^2\theta & (\gamma - 1)\cos\theta \sin\theta \\ (\gamma - 1)\cos\theta \sin\theta & -\gamma\cos^2\theta - \sin^2\theta \\ \frac{1}{2}\sin\theta & -\frac{1}{2}\cos\theta \end{pmatrix} \end{aligned} \tag{10}$$

Moreover, for i and j in $\{1, \dots N\}$ the drag torque for S_j with respect to $\mathbf{x}_i$ takes the form

$$\mathbf{M}^h_{j,\mathbf{x}_i} = \int_{S_j} (\mathbf{x}(s) - \mathbf{x}_0) \times \mathbf{f}_j(\mathbf{x}(s)) ds,$$

After computation, the torque for the j-th filament with respect to $\mathbf{x}_i$ reads

$$\mathbf{M}^h_{j,\mathbf{x}_i} \cdot \mathbf{e}_z = \eta \Delta s \begin{pmatrix} \Delta s \\ x_j - x_i \\ y_j - y_i \end{pmatrix}^T M(\theta_j) \begin{pmatrix} \dot{x}_j \\ \dot{y}_j \\ \Delta s\, \dot{\theta}_j \end{pmatrix} \tag{11}$$

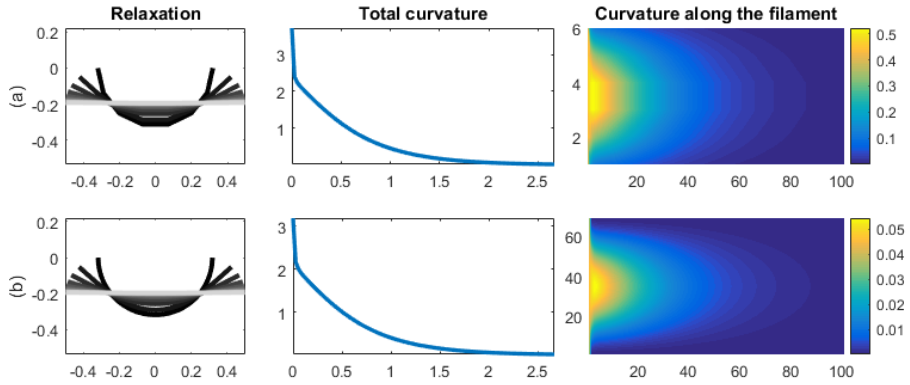

FIG. 2. Graphic visualization of the filament relaxation starting from a half-circle shape with (a) 7 and (b) 70 links. The graphs on the second colums show the total curvature with respect to time. It is very similar for both cases. The graphs on the third column show a colormap of the curvature (blue for no curvature, yellow for a high curved region) with time step in abscissa and link number in ordinate.

with

$$M(\theta) = \begin{pmatrix} -\frac{1}{2}\cos\theta & \frac{1}{2}\sin\theta & -\frac{1}{3} \\ (1-\gamma)\cos\theta\sin\theta & -\cos^2\theta - \gamma\sin^2\theta & -\frac{1}{2}\cos\theta \\ \gamma\cos^2\theta + \sin^2\theta & (\gamma-1)\cos\theta\sin\theta & -\frac{1}{2}\sin\theta \end{pmatrix}. \quad (12)$$

Elasticity

The torsional springs which connect the filament segments exert a torque $\mathbf{m}^{\text{el}}$ proportional to the shape angles α_i. This allows to match the linear elastic theory used for the continuous model. Thus,for $i \in 2 \dots N$, the torque exerted by S_{i-1} on S_i is given by

$$\mathbf{m}_i^{\text{el}} = \kappa\,\alpha_i \mathbf{e}_z = \kappa\,(\theta_i - \theta_{i-1})\mathbf{e}_z. \quad (13)$$

Let us recall the expression of the elastic torque in the continuous filament model: $\mathbf{m}(s) = E_b \frac{\partial\theta}{\partial s}\mathbf{e}_z$, E_b being the bending stiffness of the filament. By choosing

$$\kappa = \frac{NE_b}{L} = \frac{E_b}{\Delta s},$$

we get the convergence of $\mathbf{m}_i^{el}$ towards the "continuous" elastic effect when N goes to infinity. Thus, provided the stiffness of the torsional spring is chosen as above, the N-link ODE model is equivalent to the continuous filament model.

Nondimensionalization

Finally, we proceed to a nondimensionalization with respect to length scale Δs and time scale ω. This allows to factorize equations (10) and (11) by $\eta\omega\Delta s^3$, letting a new parameter appear :

$$Sp_N = \Delta s \left(\frac{\eta\omega}{\kappa}\right)^{1/3}$$

Note that, since $\kappa = E_b/\Delta s$, we get the relation

$$Sp_N = \left(\frac{Sp}{N}\right)^{4/3},$$

where Sp is the sperm number obtained in the dimensionless PDE model : $Sp = L\left(\frac{\eta\omega}{E_b}\right)^{1/4}$. For a given sperm number in the continuous model, we get a different sperm number for the ODE model in order for it to match the behaviour of the continuous filament.

Using the expressions above, we can write the ODE system as a matricial system. All the entries of the matrices, allowing a quick numerical implementation, are given in appendix VI B.

B. Comparison between the two models

The main difference between the two models consists in the time where a discretization is performed. In the first case, the base system (1)-(2) is derived into a purely analytic PDE system, then discretized in the numeric part, according to a particular numerical scheme. On the contrary, in the discrete filament case, we perform a first discretization on the filament model, allowing to integrate the equations into an ODE system – hence the term " semianalytical", that can be solved numerically with any standard scheme.

III. COMPARISON PDE VS ODE: THE RELAXATION CASE

In this section, we will show that the numerical solutions given by the N-link swimmer model converge towards those given by the PDE model.

All simulations were run on an Intel Core i5-6500 processor at 3.20 GHz, using MATLAB software.

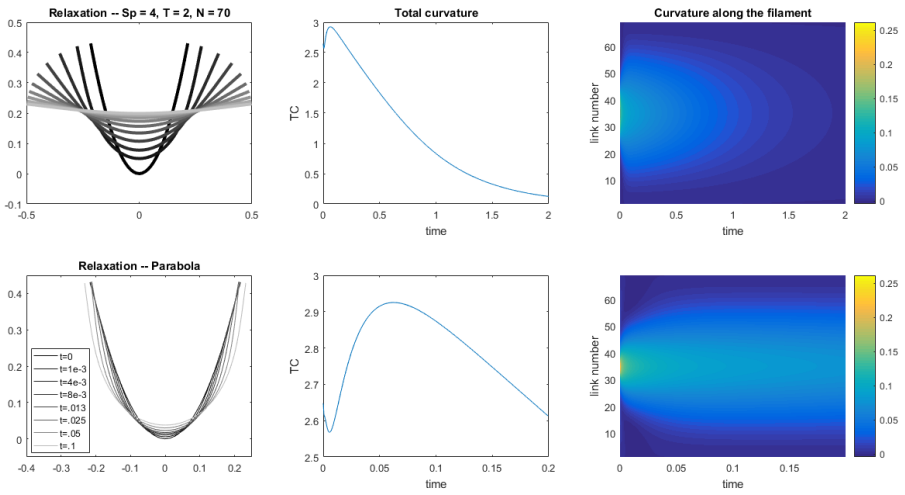

FIG. 3. Relaxation when the initial shape is a parabola arc. The second row zooms in on a smaller time interval at the start, to highlight an interesting phenomenon: at first, the sharp curvature in the middle of the filament starts travelling towards the ends, temporarily increasing the total curvature.

A. Numerical methods

For the discrete filament, a classic Runge-Kutta scheme would work for instance; however, we choose to use here the `ode15s` solver embedded in the MATLAB software. It uses a variable-order, variable-step method based on the numerical differentiation formulas (NDFs) of orders 1 to 5 [33], hence giving better performances than a standard fixed step scheme.

The numerical scheme used to deal with them in [30] is a second-order implicit-explicit scheme (IMEX) [], that treats the highest-order terms implicitly, and all the lower-order terms explicitly. Spatial and temporal discretizations are uniform. The numerical scheme is initiated with a first-order scheme, then each iteration is made of three steps:

- knowing the position of the filament $\mathbf{x}$ at time t_n, using Equation 5, we can obtain the tension and derivatives along all the filament at time t_n with eq.
- the boundary conditions allow to get the tension at time t_n at both ends of the filament
- knowing $\mathbf{x}$ and τ at time t_n, we can get $\mathbf{x}$ at time t_{n+1} along the filament, and go back to the first step.

B. Test description

We will compare the results of the two models over a relaxation test : the initial shape of the filament is set to a half-circle initial shape and the solution is computed until it is at rest, i.e. at straight position. More precisely, for the N-link filament, the initial condition for the relative angles between the segments is

$$\alpha_1(0) = \frac{\pi}{2} + \frac{\pi}{2N}, \quad \alpha_2(0) = \cdots = \alpha_N(0) = \frac{\pi}{2N}.$$

A graphic visualization of this relaxation test, for two different numbers of links, can be seen on the first column of Figure 2 (a) and (b).

C. Error criterion

In order to compare the movement of a (theoretically) continuous filament and a discrete filament, or even between two discrete filaments with different numbers of links, we need to set an invariant criterion. A good candidate for this purpose is the total curvature along the filament. It is easy to define for a continuous filament – the integral of the curvature over the filament and for a discrete filament – the sum of the relative shape angles. This criterion is invariant with respect to the geometric parametrization of the filament and also to the number of links considered in the discrete model, which makes it convenient to compare the results of two filaments with different numbers of links.

The second column of Figure 2 shows the variation of total curvature over time for the relaxation test, for filaments made of 7 links (row (a)) and 70 links (row (b)). We can see that the total curvature decreases over time, as the filament relaxes to a straight shape, corresponding to a total curvature of zero.

The total curvature is not necessarily always decreasing: when the filament is sharply curved, such as on Figure 3, it can increase at first. These cases are more numerically challenging for there are very short time scales come into play.

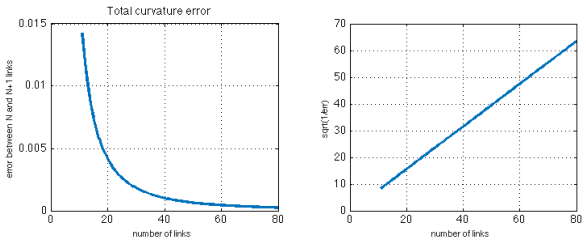

FIG. 4. Discrete total curvature error between N links and $N+1$ links, with respect to N.

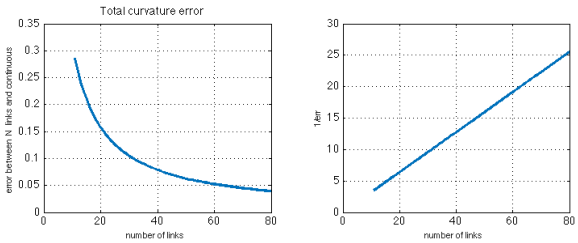

FIG. 5. Inverse of the total curvature error between N-link swimmer and continuous model, with respect to N. As one can see, the error is proportional to $1/N$.

The difference in total curvature between two given filaments can be computed over the whole relaxation time. The maximum of this difference over the time interval gives us the total curvature error criterion. Hence, we define the *total curvature error*: given $(x^N(t), y^N(t), \alpha_1^N(t), \dots, \alpha_N^N(t))$ and $(x^M(t), y^M(t), \alpha_1^M(t), \dots, \alpha_M^M(t))$ be the solutions of the system (9), for respectively N- and M-link-filaments, for some given initial conditions, over $[0, T]$, the discrete total curvature error between the two solutions reads

$$\begin{aligned} \varepsilon_{TC}^{N,M} &= \|TC_N(t) - TC_M(t)\|_{\infty,[0,T]} \\ &= \|\sum_{i=1}^N \alpha_i^N(t) - \sum_{i=1}^M \alpha_i^M(t)\|_{\infty,[0,T]}. \end{aligned}$$

The continuous equivalent of the discrete total curvature is given by the integral of the local curvature over the filament : $TC(t) = \int_0^1 \kappa(s,t)ds = \int_0^1 \|\frac{\partial^2 X(s,t)}{\partial s^2} ds\|$. The error between continuous and discrete filaments reads

$$\varepsilon_{TC}^{N,\text{cont}} = \|TC_N(t) - TC(t)\|_{\infty,[0,T]}.$$

D. Comparison between continuous and discrete models

The first numerical experiment consists in checking that the ODE model converges towards a solution when one increases the number of links. Figure 4 shows the discrete total curvature error between two successive numbers of links for the relaxation test, with Sp = 4. It decreases like $1/N^2$. The error reaches an order of magnitude of 10^{-4} from around 50 to 60 links.

In order to test the accuracy of the ODE model with respect to the number of links, we compared it against the PDE model results. For the PDE results model, we chose 100 space steps and 10^4 time steps, therefore ensuring that it would give excellent results in our case (i.e. the numerical problems that occur with this model will not occur here). This parameter choice matches the one from [30]. The comparison between the PDE and ODE models appears on Figure 5. The error decreases proportionally to the inverse of the number of links. It therefore ensures that both models give similar results numerically.

Let us now compare the computing times of both models for two relaxation tests. In Table III D, we compare the time needed to get a numerical solution for two relaxation tests:

- a relaxation from half a circle to the straight shape, used above to validate the N-link model
- a relaxation from a parabola arc to the straight shape, more challenging than the first one due to sharper initial curvature

We show the computing time for three different levels of precision and two different sperm numbers. When the sperm number is smaller, the filament is more rigid and relaxes faster, thus more difficult to solve numerically without errors. The precision level is obtained by checking the total length relative error over the solving time interval to remain within the tolerance. We chose the smallest possible time- and space steps that fit in the precision requirements, in order to get the smallest possible computing time for the PDE model.

As we can see on Table III D, the PDE model gives bad numerical performances when the filament is rigid and when the curvature is sharp. On the contrary, the discrete filament model seems to easily be able to bear sharp curvatures initially or during its movement. Indeed, by construction, the total length of the discrete filament remains constant, hence the numerical errors showing in the PDE disappear.

Let us discuss the advantages and downsides of each model. The continuous filament model, despite being theoretically closer to reality than the other, lacks numerical robustness. It gives bad performances with small sperm numbers and high curvatures. In this cases, the chosen time step has to be very small for the solution to be satisfying. On the other hand, the numerical performances of the discrete model are similar for a wide range of sperm numbers.

Another noticeable advantage of the discrete filament model is its easy implementation : it only requires to fill the matrices of the system (21), and use any ODE numerical scheme – though, as we saw above, some are much more efficient than others. On the other hand, as a PDE system, the continuous model requires a complex specific scheme.

$Sp = 4$, $T = 3$			
Test	N-link model N=70	Tolerance on total length	PDE model
Half-circle	2	1% 0.1% 0.01%	1.3 249 3750
Parabola	1.5	1% 0.1% 0.01%	90 1820 $>$ 1h
$Sp = 2$, $T = 1$			
Test	N-link model N=70	Tolerance on total length	PDE model
Half-circle	3	1% 0.1% 0.01%	97 850 $>$ 1h
Parabola	1.7	1% 0.1% 0.01%	$>$ 1h $>$ 1h $>$ 1h

TABLE I. Computing times in seconds for the two relaxation tests and two different sperm numbers.

Test	N-link model N=70	Tolerance on total length	PDE model
Oscillation Sp=4	0.9	1% 0.1% 0.01%	10 36 155
Oscillation Sp=2	1.0	1% 0.1% 0.01%	32 820 $>$ 1h

TABLE II. Computing times for the oscillation case.

To complete this overview, we consider another type of regime: an oscillation test where one end of the filament is fixed and actuated by a given sinusoidal torque. The computing times are presented in table II. Again, we can see that the more rigid the filament, the more difficult it is for the PDE model to give accurate results.

Let us state a last remark about the discrete model with very high numbers of links: artefacts occur from roughly $N = 100$, or more depending on the parameters and the initial condition. For such high values, the scheme sometimes has to run an extremely long time (at least 20 minutes, and sometimes much more) to compute a solution. We expect this phenomenon to be due to "areas" of extreme stiffness on the time interval, which requires to use an unreasonably small time step. It seems rather difficult to foresee when these bad cases are going to happen. Nonetheless, the results obtained with 30 to 80 links have a very good accuracy. Thus, there is no need to use higher numbers of links that lead to numerical artefacts.

IV. APPLICATIONS

The discrete model described in part II is a robust base material, and slight additions or modifications allow to study a wide range of problems. External forces and torques are easy to add in the model (the $\mathbf{p}$ term in Equation (2)). Without changing the principle of the numerical method, it is possible to add in various effects such as shear flows, gravity effects, electromagnetic effects, and so on, that allow to study a wide scope of problems. In the following, we describe three examples of what can be done from the base model: examining the buckling instability, drive a swimmer with an external magnetic field, and study a filament bundle.

A. Buckling

[14, 28, 30] The nature of the ODE model allows more freedom concerning the boundaries conditions and the structure of the filament. It is relatively easy to add constraints, e.g. a fixed extremity, by simply adding constraint equations to the system (9).

The buckling phenomenon for a filament occurs when one of its extremities is fixed, and the other one moves towards it. It leads to an instability : the filament will buckle in a "random" direction (see Figure 6).

As for the equations of motion, one has to add an unknown force at each end of the filament to constraint the ends. In the PDE model, this is very challenging, since there already is the inextensibility constraint. The N-link model makes it quite easier.

Let us assume that the filament is initially at rest along the (Ox) axis. To make the filament buckle, we must apply a contact force at each end of it. Let us call these forces respectively $\mathbf{f}_0 = \begin{pmatrix} f_{0x} \\ f_{0y} \end{pmatrix}$ and $\mathbf{f}_N = \begin{pmatrix} f_{Nx} \\ f_{Ny} \end{pmatrix}$. The system (9) is modified : it is now

$$\begin{cases} \sum_{i=1}^{N} \mathbf{f}_i^h & +\mathbf{f}_0 + \mathbf{f}_N & = & 0 \\ \sum_{i=1}^{N} \mathbf{m}_{i,\mathbf{x}_1}^h & +\mathbf{m}_{N,\mathbf{x}_1} & = & 0 \\ \sum_{i=2}^{N} \mathbf{m}_{i,\mathbf{x}_2}^h & +\mathbf{m}_{N,\mathbf{x}_2} & = & -\mathbf{m}_2^{\text{el}} \\ \vdots & \vdots & \vdots & \\ \mathbf{m}_{N,\mathbf{x}_N}^h & +\mathbf{m}_{N,\mathbf{x}_N} & = & -\mathbf{m}_N^{\text{el}} \end{cases} \tag{14}$$

where the $\mathbf{m}_{N,\mathbf{x}_i}$ are the moments induced by $\mathbf{f}_N$ with respect to the point $\mathbf{x}_i$:

$$\mathbf{m}_{N,\mathbf{x}_i} = (\mathbf{x}_{N+1} - \mathbf{x}_i) \times \mathbf{f}_N.$$

We now have four new scalar unknowns: f_{0x}, f_{0y}, f_{Nx}, f_{Ny}. To be able to solve the system, we need four equations, given by the buckling kinematic constraints

$$\begin{cases} \dot{x}_1 = k, \\ \dot{y}_1 = 0, \\ \dot{x}_N = 0, \\ \dot{y}_N = 0. \end{cases} \tag{14b}$$

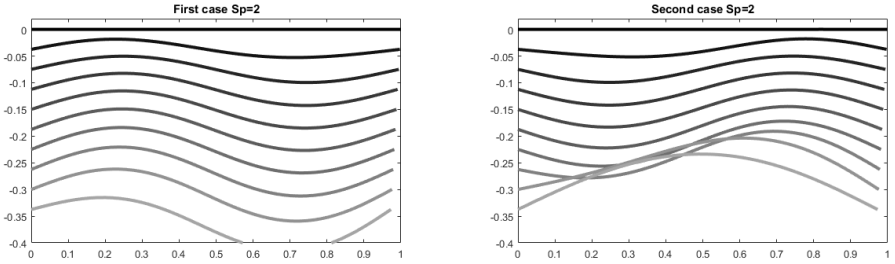

(a)$Sp = 2$

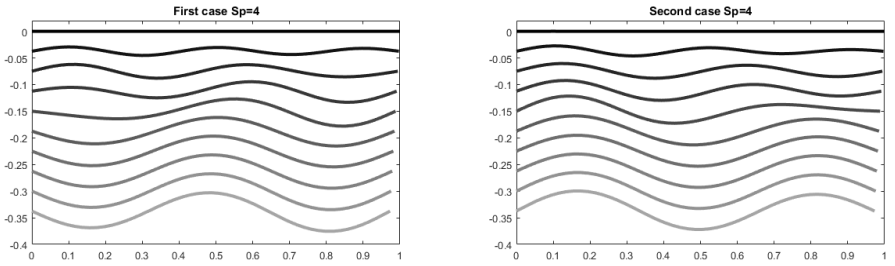

(b)$Sp = 4$

FIG. 6. Visualization of the buckling phenomenon for two different sperm numbers. The filament is displayed at regular intervals of time and translated downwards at each step to improve visibility. The randomness introduced in the initial condition leads to different outcomes.

where k is positive. We then concatenate (14) and (14b) to obtain a system of $(N+6)$ scalar equations. After the calculations, we get a system that can be expressed as follows:

$$\mathbf{A}_b\dot{\mathbf{X}}_b = \mathbf{B}_b, \tag{15}$$

where

$$\mathbf{X}_b = \begin{pmatrix} \mathbf{X} \\ \hline f_{0x} \\ f_{0y} \\ f_{Nx} \\ f_{Ny} \end{pmatrix}, \ \mathbf{B}_b = \begin{pmatrix} \mathbf{B} \\ \hline k \\ 0 \\ 0 \\ 0 \end{pmatrix}, \ \mathbf{A}_b = \left(\begin{array}{c|c} \mathbf{AQ} & \mathbf{a}^T \\ \hline \mathbf{a} & \mathbf{0} \end{array}\right), \tag{16}$$

$$\mathbf{a} = \begin{pmatrix} 1 & 0 & 0 & \dots & \dots & 0 \\ 0 & 1 & 0 & \dots & \dots & 0 \\ 1 & 0 & -\sum_{k=1}^{N} \sin\theta_k & -\sum_{k=2}^{N} \sin\theta_k & \dots & -\sin\theta_N \\ 0 & 1 & \sum_{k=1}^{N} \cos\theta_k & \sum_{k=2}^{N} \cos\theta_k & \dots & cos\theta_N \end{pmatrix}. \tag{17}$$

The expressions of $\mathbf{A}$, $\mathbf{B}$ and $\mathbf{Q}$ are recalled in Appendix VI B. As stated before, the initial set of parameters should be $\begin{pmatrix} 0 & \dots & 0 \end{pmatrix}^T$, but this is numerically impossible to deal with: $\mathbf{A}_b$ is not invertible in this situation and the numerical scheme can not start at all. We need to introduce a slight bias in the initial shape of the swimmer in order to induce the buckling numerically. The chosen initial condition for the following examples is, for a small angular parameter ϵ:

$$\mathbf{X}(0) = \begin{pmatrix} 0 & 0 & \dots & 0 & \epsilon & -2\epsilon & \epsilon & 0 & \dots & 0 \end{pmatrix}^T$$

The value of ϵ has been set to 10^{-3} in the simulations, with no visible difference when setting it at lower orders of magnitude. The sign of ϵ and the position of the first nonzero entry are chosen randomly, to reproduce the randomness of the buckling phenomenon. The results are shown on figure 7, with interesting different behaviours for different sperm numbers.

B. External effects : magnetism

Driving microswimmers with a magnetic field a relatively new and promising technique ([34, 35]). Let us go into detail on how to adapt our model to describe a magnetized filament, leading to exciting applications.

As in [31], we can assume that each link of our filament is magnetized with a magnetic moment M_i, add a uniform time-varying magnetic field in the surrounding fluid and look at the magnetic effects on the swimmer. In [31], the authors manage to make a swimmer move forward and turn by applying a sinusoidal field.

The torque exerted by a magnetic field will appear in the system (1)-(2) as the external moment $\mathbf{p}$, that we assumed to be zero until now. We now assume that a time-varying magnetic field $\mathbf{H}(t) = \begin{pmatrix} H_x(t) \\ H_y(t) \end{pmatrix}$ exerts a torque on the segment S_i proportional to its magnetization M_i:

$$\mathbf{m}_i^m = M_i \mathbf{e}_{i,\parallel} \times \mathbf{H}.$$

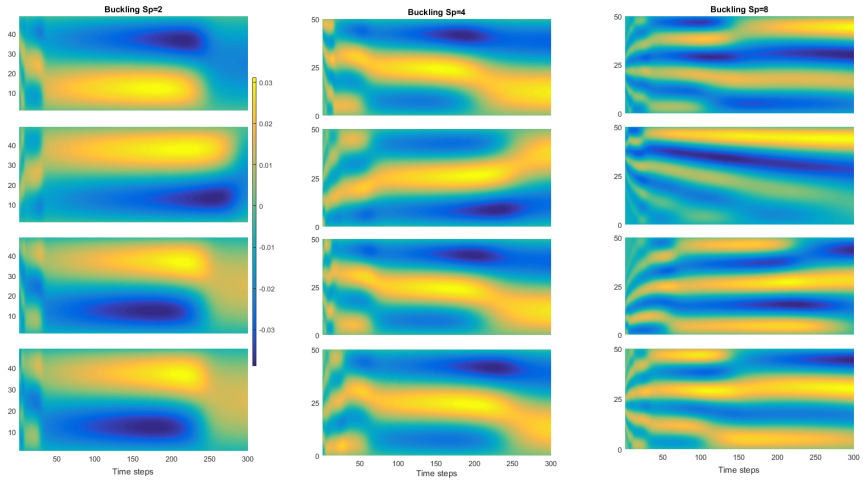

(a)Low Sp, $T = 0.5$ (b)Medium Sp, $T = 1$ (c)High Sp, $T = 2$

FIG. 7. Results from the buckling simulation. The graphs show time on the x-axis (note that the total time T, written on bottom of each column, varies with sperm number) and link number (discrete arclength) on the y-axis. The colours show the curvature over time, from blue for a highly negative curvature to yellow for a highly positive one. The filament quickly takes a waveform with less and less waves as time goes on. The higher the sperm number is, the longer it takes for the waves to vanish (note that the total time on the graphs is longer as the sperm number increases). Moreover, the initial bias leads to different outcomes: see, for instance, on the left column, how the top graph is almost the symmetric image to the bottom two – the curvature is the opposite. The characteristic times for each regime seem to be similar, but more variability seems to appear as Sp increases.

The system (9) then reads

$$\begin{cases} \sum_{i=1}^{N} \mathbf{f}_i^h &= 0 \\ \sum_{i=1}^{N} \mathbf{m}_{i,\mathbf{x}_1}^h &= \mathbf{m}_1^m \\ \sum_{i=2}^{N} \mathbf{m}_{i,\mathbf{x}_2}^h &= \mathbf{m}_2^m - \mathbf{m}_2^{\text{el}} \\ \vdots & \vdots \quad \vdots \\ \mathbf{m}_{N,\mathbf{x}_N}^h &= \mathbf{m}_N^m - \mathbf{m}_N^{\text{el}} \end{cases} \tag{18}$$

In the matricial form (21), one just has to add to the second member $\tilde{\mathbf{B}}$ the magnetic effect vector $\mathbf{C} = \begin{pmatrix} c_1 & \dots & c_N \end{pmatrix}^T$, with $c_1 = c_2 = 0$ and $\forall i \in \{3, \dots, N+2\}$,

$$c_i = \sum_{k=i}^{N} M_k (H_y \cos\theta_k - H_x \theta_k).$$

The magnetic field can be chosen freely, allowing to observe a lot of different behaviours in the filament's movement. The main goal for a magnetic robot is to be able to move efficiently in a given direction. Figure 8 shows an example of a partially magnetized swimmer on which we applied a sinusoidal magnetic field.

The research in the control theory field about magnetic swimmers is very dynamic, and a lot of open problems remain, regarding controllability as well as optimal control. Given a magnetized swimmer, can we find the best magnetic field that will drive it in a given direction as fast as possible? The discrete model gives a good starting point to numerically study these kind of problems.

C. The counterbend phenomenon

Due to its specific structure, the flagellum of a sperm cell does not behave as a single passive elastic filament. Elastic-linking proteins inside the flagellum generate tangential forces when it bends. It has been observed that the induction of curvature in one section of a passive sperm flagellum instigates non-trivial compensatory counter-curvature elsewhere [36]. This is called the counterbend phenomenon and has been dealt with in numerous studies [28, 36, 37], including [19], in which the flagellum is modeled as a "bundle" made of two thin filaments linked to each other. When this bundle bends, the links between the two filaments induce a reaction due to the sliding displacement between them. With this effect, an angular actuation at one end of the filament bundle generates a second oscillation at the free end of the filament. We propose to reproduce the results obtained in that paper with the N-link model.

The authors in [19] model the sliding reaction with a torque proportional to the sliding displacement, i.e. the angle between the tangent lines to the filament at the current point and at the fixed end. In our discrete model, this translates to a couple applied to each link:

$$\mathbf{T}_i^s = \kappa'(\theta_i - \theta_1), \tag{19}$$

where κ' is a stiffness constant. Adding this term to the nondimensionalized system (9), we get a new dimensionless constant $K = \frac{\kappa'}{\kappa}$ that represents the balance between

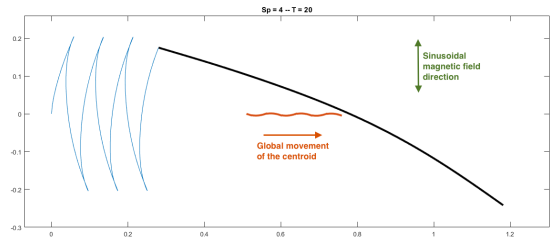

FIG. 8. Example of magnetic drive with a sinusoidal orthogonal magnetic field. One fifth of the length of the swimmer is nonmagnetized, and the other part is constantly magnetized. The black line is the position of the filament at the end of the simulation. The blue and orange lines respectively show the trajectory of the nonmagnetized end and the centroid of the filament.

the elastic effects that are internal to the filament, and the sliding effects that come from the bundle structure.

The results of the simulations are visible on figure 9. To match the parameters chosen in [19], we chose $\mathrm{Sp} = 7$, $K = \frac{1}{5}$ and applied a forced oscillation with amplitude 0.4362 rad to one end of the filament. The second travelling wave generated at the free end of the filament appears on Figure 9(b). The results are in very good agreement with the ones obtained in [19]-Fig.2, and again improved significantly the computing time.

V. CONCLUSIONS

We studied inertialess fluid-structure interaction of inextensible filaments. The nonlinear coupling between the geometry of deformation and the physical effects invariably result on intricate governing equations that negotiate elastohydrodynamical interactions with nonholonomic constraints, as a direct consequence of the filament inextensibility. This triggers numerical instabilities and require penalization methods and high-order spatiotemporal propagators.

We exploit the the momentum balance in the asymptotic limit of small rod-like elements which are integrated semi-analytically. This bypasses the nonlinearities arising via the inextensibilty constraint, avoiding in this way the need of Langrange multipliers. The equivalence between the continuous and asymptotic model allows a direct comparison between the two formalisms. The nature of the asymptotic approximation entails that coarse discretisation is possible while having a higher precision when compared with the continuous approach.

The asymptotic model observed to be numerically stable in situations in which the continuous formalism has a very poor performance, while the coarse structure guarantees faster computations, over than a hundred times faster than previous schemes. The asymptotic model is simple and intuitive to implement, and generalisations for complex interaction of multiple rods, Brownian polymer dynamics, active filaments and non-local hydrodynamics are straightforward.

ACKNOWLEDGMENTS

The authors were partially funded by the CNRS through the project Défi InFIniti-AAP 2017.

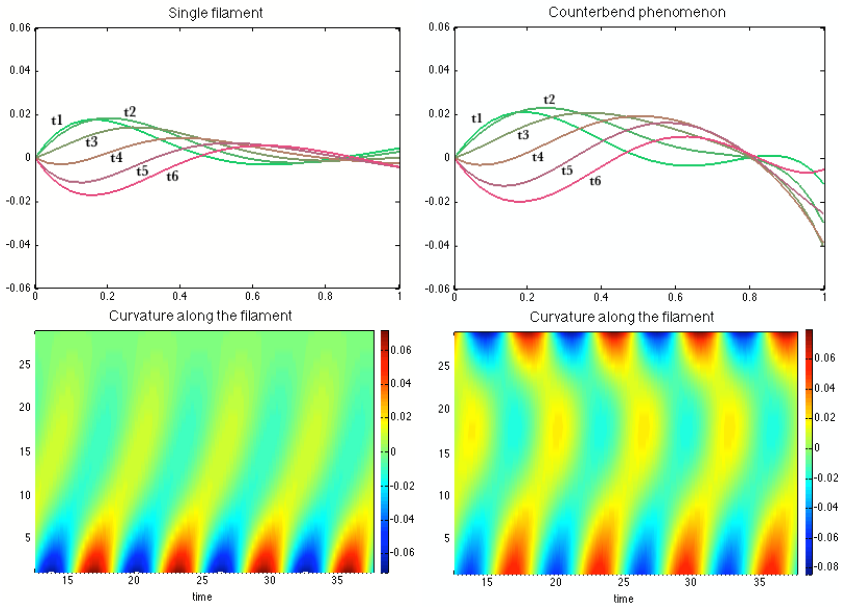

(a) (b)

FIG. 9. Simulation of the counterbend phenomenon. The color plots on the bottom show the curvature with respect to the time in x and the link number in y (here $N = 30$). The left column shows an oscillation applied to the base model. The right column shows the same oscillation applied to the bundle model. The travelling curvature wave generated by the actuation is visible at the bottom of both color plots. One can see the second travelling wave that appears at the free end of the filament in the bundle case, at the top of the color plot.

VI. APPENDIX

A. Parametrization of the discrete filament

The discrete filament can be fully described with two different sets of parameters (see figure 1) :

- the $N+2$ parameters $\mathbf{X} = (x_1, y_1, \theta_1, \alpha_2, \dots, \alpha_N)$.
- the $3N$ parameters $\mathbf{X}_{3N} = (x_1, \dots, x_N, y_1, \dots, y_N, \theta_1, \dots, \theta_N)$,

The second set is not optimal, since it uses $3N$ parameters where $N+2$ are enough, but it makes the computations easier. Going from $\mathbf{X}$ to $\dot{\mathbf{X}}_{3N}$ can easily be done with the following transformation matrices :

$$\dot{\mathbf{X}} = \tilde{\mathbf{P}}\dot{\mathbf{X}}_{3N} \quad \text{and} \quad \dot{\mathbf{X}}_{3N} = \tilde{\mathbf{Q}}\dot{\mathbf{X}}$$

with

$$\tilde{\mathbf{P}} = \left(\begin{array}{cccc|cccc|c} 1 & 0 & \dots & 0 & 0 & \dots & 0 & & \\ 0 & \dots & 0 & 1 & 0 & \dots & 0 & & 0_{2,N} \\ \hline & & & & & & & 1 & 0 \dots \quad \dots \quad 0 \\ & & & & & & & -1 & 1 \quad 0 \quad \dots \quad 0 \\ & 0_N & & & & 0_N & & 0 & -1 \quad 1 \quad \ddots \quad \vdots \\ & & & & & & & \vdots & \ddots \quad \ddots \quad \ddots \quad \vdots \\ & & & & & & & 0 & \dots \quad 0 \quad -1 \quad 1 \end{array}\right)$$

and

$$\tilde{\mathbf{Q}} = \left(\begin{array}{cc|ccc} 1 & 0 & & & \\ \vdots & \vdots & & \tilde{Q}_1 & \\ 1 & 0 & & & \\ \hline 0 & 1 & & & \\ \vdots & \vdots & & \tilde{Q}_2 & \\ 0 & 1 & & & \\ \hline & & 1 & 0 \dots & 0 \\ & & 1 & 1 \quad \ddots & \vdots \\ & 0_{N,2} & \vdots & \ddots & 0 \\ & & 1 & \dots & 1 \end{array}\right), \tag{20}$$

where $\tilde{Q}_1$ and $\tilde{Q}_2$ are $N \times N$ matrices whose elements are given by the general formula

$$q_1^{i,j} = -\Delta s \sum_{k=j}^{i-1} \sin\left(\sum_{m=1}^{k} \alpha_m\right)$$
$$q_2^{i,j} = \Delta s \sum_{k=j}^{i-1} \cos\left(\sum_{m=1}^{k} \alpha_m\right),$$

with $q_1^{i,j} = q_2^{i,j} = 0$ if $i \geq j$. We are using "tildes" in order to recall that we have not performed the nondimensionalization yet.

B. Matricial form of the ODE system

Using the explicit expressions of the different contributions (10), (11) and (13), and after nondimensionalizing, we can rewrite the system (9) as a matricial system with respect to the parameters:

$$Sp_N^3 \mathbf{A}\mathbf{Q}\dot{\mathbf{X}} = \mathbf{B}. \tag{21}$$

Let us give the detailed content of the different terms.

- The matrix $\mathbf{A}$ is a $(N+2) \times 3N$ matrix whose coefficients are given, for all i in $\{1, \dots N\}$ and j in $\{i, \dots, N\}$, by

$$\begin{array}{ll} a_{1,i} = -\cos^2\theta_i - \gamma \sin^2\theta_i; & a_{2,i} = (\gamma-1)\cos\theta_i \sin\theta_i; \\ a_{1,N+i} = (\gamma-1)\cos\theta_i \sin\theta_i; & a_{2,N+i} = -\gamma\cos^2\theta_i - \sin^2\theta_i; \\ a_{1,2N+i} = \frac{1}{2}\sin\theta_i; & a_{2,2N+i} = -\frac{1}{2}\cos\theta_i; \end{array}$$

$$\begin{array}{l} a_{i+2,j} = v(\tilde{\mathbf{x}}_i, \tilde{\mathbf{x}}_j)\, M_1(\theta_j); \\ a_{i+2,N+j} = v(\tilde{\mathbf{x}}_i, \tilde{\mathbf{x}}_j)\, M_2(\theta_j); \\ a_{i+2,2N+j} = v(\tilde{\mathbf{x}}_i, \tilde{\mathbf{x}}_j)\, M_3(\theta_j); \end{array}$$

  where $v(\tilde{\mathbf{x}}_i, \tilde{\mathbf{x}}_j) = \begin{pmatrix} 1 & \tilde{x}_j - \tilde{x}_i & \tilde{y}_j - \tilde{y}_i \end{pmatrix}$ and M_1, M_2, M_3 are the columns of the matrix (12). If $j < i$, then $a_{i+2,j} = a_{i+2,N+j} = a_{i+2,2N+j} = 0$.

- $\mathbf{Q}$ is the nondimensionalized version of the transformation matrix (20). It is defined by replacing $\tilde{Q}_1$ and $\tilde{Q}_2$ with $Q_1 = \tilde{Q}_1/\Delta s$ and $Q_2 = \tilde{Q}_2/\Delta s$ in the expression of $\tilde{\mathbf{Q}}$.

- $\mathbf{B}$ is a column vector of size $N+2$, given by

$$\mathbf{B} = \begin{pmatrix} 0 & 0 & 0 & \alpha_2 & \dots & \alpha_N \end{pmatrix}^T.$$

[1] SS Antman. *Nonlinear Problems of Elasticity*, volume 107 of *Applied Mathematical Sciences*. Springer, 2005.

[2] B. Alberts. *Molecular Biology of the Cell*. Garland Science, New York, 2002.

[3] J. Howard. *Mechanics of motor proteins and the cytoskeleton*. Sinauer Associates Sunderland, MA, 2001.

[4] H. Gadêlha, E. A. Gaffney, D. J. Smith, and J. C. Kirkman-Brown. Nonlinear instability in flagellar dynamics: a novel modulation mechanism in sperm migration? *Journal of The Royal Society Interface*, 7:1689–, 2010.

[5] Sbastien Camalet, Frank Jülicher, and Jacques Prost. Self-organized beating and swimming of internally driven filaments. *Phys. Rev. Lett.*, 82:1590, 1999.

[6] L. Bourdieu, T. Duke, M. B. Elowitz, D. A. Winkelmann, S. Leibler, and A. Libchaber. Spiral defects in motility assays: A measure of motor protein force. *Phys. Rev. Lett.*, 75:176–179, 1995.

[7] R. E. Goldstein and S. A. Langer. Nonlinear dynamics of stiff polymers. *Phys. Rev. Lett.*, 75:1094–1097, 1995.

[8] H. C. Fu, C. W. Wolgemuth, and T. R. Powers. Beating patterns of filaments in viscoelastic fluids. *Phys. Rev. E*, 78:041913–041925, 2008.

[9] T. S. Yu, , E. Lauga, and A. E. Hosoi. Experimental investigations of elastic tail propulsion at low reynolds number. *Phys. Fluids*, 18:0917011–0917014, 2006.

[10] Sarah D. Olson, Sookkyung Lim, and Ricardo Cortez. Modeling the dynamics of an elastic rod with intrinsic curvature and twist using a regularized Stokes formulation. *Journal of Computational Physics*, 238:169–187, April 2013.

[11] A. K. Tornberg and M. J. Shelley. Simulating the dynamics and interactions of flexible fibers in stokes flows. *J. Comput. Phys.*, 196:8–40, 2004.

[12] Vasily Kantsler and Raymond E. Goldstein. Fluctuations, Dynamics, and the Stretch-Coil Transition of Single Actin Filaments in Extensional Flows. *Physical Review Letters*, 108(3):038103, January 2012.

[13] Tim Sanchez, Daniel T. N. Chen, Stephen J. DeCamp, Michael Heymann, and Zvonimir Dogic. Spontaneous motion in hierarchically assembled active matter. *Nature*, 491(7424):431–434, November 2012.

[14] Clifford P. Brangwynne, Frederick C. MacKintosh, Sanjay Kumar, Nicholas A. Geisse, Jennifer Talbot, L. Mahadevan, Kevin K. Parker, Donald E. Ingber, and David A. Weitz. Microtubules can bear enhanced compressive loads in living cells because of lateral reinforcement. *J Cell Biol*, 173(5):733–741, June 2006.

[15] Franck Plouraboue, Ibrahima Thiam, Blaise Delmotte, Eric Climent, PSC Collaboration, et al. Identification of internal properties of fibers and micro-swimmers. In *APS Meeting Abstracts*, 2016.

[16] Claus Heussinger, Felix Schüller, and Erwin Frey. Statics and dynamics of the wormlike bundle model. *Phys. Rev. E*, 81(2):021904, Feb 2010.

[17] M. M. A. E. Claessens, C. Semmrich, L. Ramos, and A. R. Bausch. Helical twist controls the thickness of f-actin bundles. *Proceedings of the National Academy of Sciences*, 105(26):8819–8822, 2008.

[18] Mireille MAE Claessens, Mark Bathe, Erwin Frey, and Andreas R Bausch. Actin-binding proteins sensitively mediate f-actin bundle stiffness. *Nature materials*, 5(9):748–753, 2006.

[19] Rachel Coy and Hermes Gadelha. The counterbend dynamics of cross-linked filament bundles and flagella. *arXiv:1703.04179 [physics]*, March 2017. arXiv: 1703.04179.

[20] Eric Lauga and Thomas R Powers. The hydrodynamics of swimming microorganisms. *Reports on Progress in Physics*, 72(9):096601, 2009.

[21] E.M. Purcell. Life at low reynolds number. *Am. J. Phys.*, 45:3, 1977.

[22] M Hines and J J Blum. Bend propagation in flagella. I. Derivation of equations of motion and their simulation. *Biophysical Journal*, 23(1):41–57, July 1978.

[23] Eric Lauga and Thomas R. Powers. The hydrodynamics of swimming microorganisms. *Reports on Progress in Physics*, 72(9):096601, September 2009. arXiv: 0812.2887.

[24] Thomas R Powers. Dynamics of filaments and mem-

branes in a viscous fluid. *Reviews of Modern Physics*, 82(2):1607, 2010.

[25] Michael J Shelley and Jun Zhang. Flapping and bending bodies interacting with fluid flows. *Annual Review of Fluid Mechanics*, 43:449–465, 2011.

[26] Christopher Brennen and Howard Winet. Fluid mechanics of propulsion by cilia and flagella. *Annual Review of Fluid Mechanics*, 9(1):339–398, 1977.

[27] M. Hines and J. J. Blum. Bend propagation in flagella. II. Incorporation of dynein cross-bridge kinetics into the equations of motion. *Biophysical Journal*, 25(3):421–441, March 1979.

[28] H. Gadêlha, E. A. Gaffney, and A. Goriely. The counterbend phenomenon in flagellar axonemes and cross-linked filament bundles. *Proceedings of the National Academy of Sciences*, July 2013.

[29] J. Gray and J. Hancock. The propulsion of sea-urchin spermatozoa. *J. Exp. Biol.*, 32(4):802–814, 1955.

[30] H. Gad?lha, E. A. Gaffney, D. J. Smith, and J. C. Kirkman-Brown. Nonlinear instability in flagellar dynamics: a novel modulation mechanism in sperm migration? *Journal of The Royal Society Interface*, page rsif20100136, May 2010.

[31] François Alouges, Antonio DeSimone, Laetitia Giraldi, and Marta Zoppello. Can magnetic multilayers propel artificial microswimmers mimicking sperm cells? *Soft Robotics*, 2(3):117–128, 2015.

[32] L. Giraldi and J.-B. Pomet. Local controllability of the two-link magneto-elastic micro-swimmer. *Accepted in Transaction on Automatic Control*, 2016.

[33] Lawrence F Shampine and Mark W Reichelt. The Matlab ODE suite. *SIAM Journal on Scientific Computing*, 18(1):1–22, 1997.

[34] F. Alouges, A. DeSimone, L. Giraldi, and M. Zoppello. Purcell swimmer controlled by external magnetic fields. *Preprint submitted*, 2015.

[35] R??mi Dreyfus, Jean Baudry, Marcus L. Roper, Marc Fermigier, Howard A. Stone, and J??r??me Bibette. Microscopic artificial swimmers. *Nature*, 437(7060):862–865, October 2005.

[36] Charles B Lindemann, Lisa J Macauley, and Kathleen A Lesich. The counterbend phenomenon in dynein-disabled rat sperm flagella and what it reveals about the interdoublet elasticity. *Biophysical journal*, 89(2):1165–1174, 2005.

[37] Dominic W Pelle, Charles J Brokaw, Kathleen A Lesich, and Charles B Lindemann. Mechanical properties of the passive sea urchin sperm flagellum. *Cytoskeleton*, 66(9):721–735, 2009.